Oxidized Cellulose Nanofibers Decorated with Magnetite as Efficient Bioadosrbent for Organic Dyes

Ahmed Salama, Ragab Abouzeid, Benedicte Prelot, Mohamed Diab, Marwa Assaf, Peter Hesemann

Oxidized cellulose nanofibers decorated with magnetite as efficient bioadsrbent for organic

Ahmed Salama[1] , Ragab Abouzeid [1,*], Benedicte Prelot [2], Mohamed Diab[1], Marwa Assaf [2,] and Peter Hesemann[2]

[1] Cellulose and Paper Department, National Research Centre, 33 El-Bohouth St., Dokki, Giza, P.O. 12622, Egypt
[2]Institut Charles Gerhardt de Montpellier, UMR CNRS 5253 Université de Montpellier-CNRS-ENSCM, Campus CNRS, 1919 route de Mende, 34293 Montpellier Cedex 05, France
*Correspondence: (r_abouzeid2002@yahoo.com

Abstract: This article describes the immobilization of magnetite (Fe_3O_4) nanoparticles on TEMPO-oxidized cellulose nanofiber (TEMPO-CNF) through the co-precipitation of iron salts by the alkaline medium. TEMPO-CNF and TEMPO-CNF/Fe_3O_4 were confirmed by XRD, TGA, SEM, TEM, BET, and AFM. Characterization of the samples successfully showed the preparation of cellulose nanofibers with a diameter ranging from 10-15 nm and homogenous and uniform magnetic nanoparticles with a diameter of ~ 10 nm. The ability of the synthesized nanocomposite for methylene blue (MB) adsorption, as a cationic dye model, was examined. At pH 7, the highest adsorption efficiency was observed. The isotherm, kinetic models, and enthalpic contributions were calculated to evaluate adsorption experiments. With an adsorption capacity of around 303 mg/g, pseudo-second-order, and Langmuir isotherm provided the best interpretation adsorption process. In addition, the thermodynamics parameters have been evaluated from direct measurement based on Isothermal Titration Calorimetry. The current results showed that TEMPO-CNF/Fe_3O_4 nanocomposite is a promising green bioadsorbent for organic dye removal for water purification.

Keywords: Cellulose nanofiber (CNF), Magnetite, Nanocomposites, Methylene Blue (MB), adsorption

1. Introduction

Many industries including textile, clothing, and printing produced large quantities of dyes. The majority of these dyes are toxic, carcinogenic, mutagenic, and considerably may affect aquatic life even at low concentrations. Humans and marine life can be adversely affected by toxic effluents unless they are not removed before their release. Moreover, dyestuff wastewater is not easy to be removed since its recalcitrant has strong resistance to aerobic digestion and resist oxidation

processes [1]. Dyes removal from wastewater is carried out by numerous processes such as nano-filtration, ozonation, coagulation, electrocoagulation, photocatalytic degradation, and chemical precipitation and adsorption. However, the adsorption technique appeared as a more cost-effective, efficient, feasible, and environmentally friendly adsorbent for a broad range of pollutants [2–4]. The adsorption method does not yield secondary pollution, consumes less energy, and has efficient adsorption capacity. In the case of dyes, the use of various types of materials has been successfully investigated with purely organic materials (i.e., mainly resins [5]), inorganic adsorbents (oxides [6], layered materials [7,8]), or hybrid materials such as chitosan/silica composite [9]. Composite materials which combine polysaccharides with active reagents are suitable and promising materials for adsorption especially these composite materials containing inorganic nanomaterials [10–14]. Cellulose has recently emerged as an economic and sustainable polymer for preparing composite materials suitable for organic pollutants adsorption [15,16] or photodegradation. Moreover, cellulose is economically practicable since it can be modified through various chemical processes [17,18]. Cellulose could be used as a substitute for exchanging conventional, expensive, and environmentally toxic adsorbents [19]. Modification of cellulose improves its adsorption efficiency and its application in different mediums and illustrates the good potential for the elimination of numerous organic chemicals [20,21]. Several compounds, including metals, metal oxides, organic acids, bases and oxidizing agents, etc, can be utilized for cellulose modification [22]. These techniques vary in their effectiveness for preparing efficient adsorbents. Mechanisms involved in the sorption process, and the performance of the adsorbents, mainly depend on the type of modifications and together with characteristics of the wastewater. Cellulose considered a semicrystalline polymer, consists of amorphous and crystalline parts. Cellulose nanomaterials include microcrystalline, nanocrystalline, nanowhiskers, nanofibrils, bacterial cellulose, and combinations of these material types [23,24]. Amorphous regions is reported as structural weakness regions which could be attacked by acid. The individual short monocrystalline nanoparticles known as cellulose nanocrystals are formed with a diameter of 4-10 nm and a length of 50-200 nm. Cellulose nanomaterials could be prepared from cellulose pulp through acid hydrolysis. They have shown fascinating properties such as large specific surface area, high abundance, high mechanical properties, and degree of functionality [25]. Nanocomposites have been applied as feasible and efficient technique in wastewater treatment [26–28] with the particular use of magnetic

nanoparticles showing great potential [29]. Cellulose/magnetite nanocomposites made-up through the precipitation of magnetite onto the functionalized cellulose surface can be prepared utilizing distinct inorganic and organic acids [30]. For example, TEMPO-CNF grafted acrylic acid followed by crosslinking with amino-functionalized magnetite was investigated as adsorbent for heavy metal ions [13]. Abouzeid et al. conducted a study which demonstrated that combining sodium alginate, a natural and biodegradable polymer matrix, with activated charcoal, renowned for its exceptional adsorption properties of methylene blue dye [31]. Alekseeva et al. [32] synthesized and studied the chemical, and magnetic properties of the hydroxyethyl cellulose/bentonite/magnetite nanocomposite. Moreover, the authors studied the optical, mechanical, and antifungal activity of hydroxyethyl cellulose/bentonite/magnetite films. X-ray diffraction analysis revealed that the interlayer distance expanded to 1.8 nm due to the intercalation of cellulose derivatives in clay cavities owing to the intercalation of polymer molecules. Functionalized nanofiber networks of cellulose and chitosan, packed in minicolumns were investigated for adsorption of trace quantities of metal ions such as Cd (II), and Pb (II) present in aqueous solutions. Trace metals in water were imperceptible as the concentrations were lower than identification limits. The purification process through the functionalized bio-sorbents in cartridges improved the recognition of the metal ions [33]. Kloster et al. [34] prepared chitosan/nano magnetite composite films by the one-step in situ co-precipitation (solvent-casting) method. It was concluded that the magnetic behavior for prepared nanocomposite was achieved at more than 2 wt% of the composite to magnetite content. F. Cesano et al., synthesized chitosan/magnetite by co-precipitation of iron oxide in the presence of chitosan which acts as both dispersant and stabilizing matrix in a one-step method [26]. It was observed that the preparation process is simple and can be effectively utilized for example to adsorb pollutants from solid and liquid media due to its exact magnetic properties. Chitosan/magnetite multifunction with polythiophene and phosphate groups was applied as careful and efficient removal of Hg (II) was studied [35]. In addition, Bezdorozhev et al. [36] reported the synthesis of magnetic properties of chitosan/magnetite naanocomposites that were developed by chemically combining magnetite nanoparticles with chitosan. They investigated the effect of different synthesis variables, including time, iron ions, and chitosan concentrations, on the nanocomposites' shape. Results showed that magnetite-chitosan nanostructures of spherical shape and particle size of (9–18 nm) were formed. The achieved magnetite-chitosan

nanostructures can be utilized in numerous medical purposes. The synthesis of magnetic nanoparticle (Fe3O4) incorporated carboxymethyl cellulose (CMC) hydrogel nanocomposites (CMC-Fe3O4) using in-situ mineralization of Fe2+/Fe3+ ions in a hydrogel network was studied. The study investigated the potential of these nanocomposites in removing methylene blue (MB) from aqueous solutions by utilizing the magnetic property of the nanocomposites [37]. Novel magnetic chitosan/Al_2O_3/iron oxide nanoparticles were also prepared and applied as an adsorbent with high adsorption capacity in the removal of Methyl Orange. The best adsorbent amount was estimated to be 0.4 g. L-1 and the adsorption method was effective in a wide pH range of 4–10. The current study aims to prepare TEMPO-CNF/Fe_3O_4 nanocomposite through the co-precipitation technique. The prepared nanocomposite was characterized and investigated as a versatile adsorbent for the removal of cationic dyes from polluted water. Solution pH, contact time, and initial concentration were examined to identify the optimum conditions required for dye adsorption. A thermodynamic study was also carried out. A thermodynamic study based on direct calorimetric measurements was also carried out.

2. Experimental part

2.1 Materials

Bagasse fiber delivered by the Egyptian company Qena Company of Paper Industry. Sodium metaperiodite ($NaIO_4$), sodium bromide (NaBr), 2,2,6,6-tetramethylpiperidine-1-oxyl (TEMPO), ferric chloride ($FeCl_3$) and ferrous sulfate ($FeSO_4$) and methylene blue (MB) were supplied from Sigma Aldrich. Other chemicals of analytical grade were used without further purification.

2.2. TEMPO-oxidized cellulose nanofiber preparation

Bleached bagasse pulp was oxidized via the TEMPO oxidation method as previously described [38]. In brief, 25 g of cellulose pulp was suspended in 2.5 L distilled water for 30 min using mechanical stirring. TEMPO (1.0 g) and sodium bromide (10 g) were combined to previous suspension followed by the addition of 300 ml of $NaClO_2$ (15%). The oxidized cellulose was centrifuged, and the supernatant was purified using dialysis against deionized water. Mechanical defibrillation of the TEMPO-oxidized cellulose-using Masuko grinder was done to prepare TEMPO-CNF.

2.3. TEMPO-CNF/magnetite nanocomposite preparation

TEMPO-CNF/Fe_3O_4 nanocomposite was prepared through the co-precipitation technique as previously reported by Ngenefeme et al., 2013. Shortly, 0.15 g (dry weight) of T-CNF and 5.3 g of $FeCl_3$ were placed in contact with 13 ml of deoxygenated and purified water [39]. Likewise, 0.2 g of T-CNF and 2.7 g of $FeSO_4$ were separately dissolved in 13 mL of deoxygenated water. The two solutions were stirred overnight, and after that, they were mixed and deoxygenated for 15 minutes. 2 M of ammonium solution was dropwise until the black color appears due to the precipitation of magnetite. The product that was made was washed until it was neutral. The remaining material was then freeze-dried to process complete dehydration.

2.4. Studies of batch adsorption

For removing organic dyes from wastewater, the T-CNF/Fe_3O_4 nanocomposite was made and tested. Adsorption experiments were performed at 25 ^{o}C, using an aqueous solution containing 50 mg of T-CNF/Fe_3O_4 in 50 mL distilled water. The effect of pH was calculated using 100 ppm as the initial MB concentration and 120 minutes of equilibrium time. The pH was adjusted for both 3 and 8 using hydrochloric acid or sodium Hydroxide aqueous solutions. The kinetics was evaluated also with 100 mg/L as the initial dye concentration, and at pH fixed at 7. For the determination of the complete adsorption isotherm, trials were conducted out at pH 7 and a contact time (24h). Different concentration solutions of MB (25-1000 ppm) were used. UNICO UV-2000 spectrophotometer estimated solution absorbance and MB content. For desorption study, MB-loaded nanocomposite was agitated with 10 mL of 5% (v/v) acetic acid and methanol for 24 h. The adsorbent was dried at 60 ^{o}C and adsorption–desorption cycle was repeated three times.

2.5. Thermodynamic study

Using a TAM III multichannel calorimetric apparatus with nanocalorimeters and a Micro Reaction System, Isothermal Titration Calorimetry (ITC) computations were performed (TA Waters). ITC tests were performed at 298 K in Hastelloy cells with 800 µL of suspension containing 2.5 mg of TEMPO-CNF/Fe_3O_4 material in water. They consist of 23 successive injections of 10 seconds with 10 µL of a 10mM MB solution. The device is supplied with a gold paddle stirrer utilized at 90 rpm to ensure the homogeneity of the mixture. Between injections, the system is allowed to stabilize for 45 minutes. Similar conditions are used to evaluate the dilution effect (without nanocomposite) and compared with the raw measurements on TEMPO-

CNF/Fe_3O_4. Experiments were done in triplicate. The heat effects were determined after suitable subtraction of the dilution effect, and then for each dose, it was correlated to the actual amount adsorbed from the isotherm. [40].

2.6. Samples Characterization

Using various methods, the prepared samples were characterized. SEM was conducted using a Model Quanta 250 FEG (Field Emission Gun) equipped with an EDX Unit (Energy Dispersive X-ray Analyses) and 20 K of accelerating voltage. On a PerkinElmer TGA thermogravimetric, thermogravimetric technique was utilized. AFM Multimode (DI, Veeco, Instrumentation Group) was done in tapping mode using multi-130 tips. Before analysis, a T-CNF suspension was mixed with water and dropped immediately on the mica surface for four hours.

3. Results and Discussion.

3.1. TEMPO-CNFs characterization

TEMPO-CNFs were synthetized from bleached bagasse pulp, which, in comparison to other annual plants, is a good source of cellulose [25]. The morphology of TEMPO-CNFs was explored utilizing AFM. Figure 1 (a) demonstrates that the diameter of TEMPO-CNFs differs from 6 to 15 nm and the length exhibited several micrometers, these dimensions are consistent with our earlier research and provide evidence that the TEMPO-CNFs have a uniform structure [38,41]. FT-IR of TEMPO-CNFs was revealed in figure 2(b), the broad peak at 3400 cm^{-1} assigns to stretching vibrations of OH groups. The absorption peak at 1750 cm^{-1} is related to the C=O stretching vibration because of TEMPO oxidation. In addition to the absorbed water's O–H bending vibration, carboxylate groups also contribute to the peak at 1640 cm^{-1}. The peak at 1060 cm^{-1} is correlated with C-O stretching vibrations. The X-ray diffraction patterns of TEMPO-CNFs, figure 2 (C), displays cellulose I with crystalline peaks at about 2θ = 18, 23, and 34.6° which refer to (110) and (200) and (004) plane. The crystallinity index values of the samples were calculated according to Segal et al. using Equation below:

$$C.I.(\%) = \frac{I_{200} - I_{am}}{I_{200}} \times 100 \qquad (2)$$

wherein I_{002} is the intensity of diffraction peak of (200) lattice plane, and Iam is the intensity of the amorphous background scatter measured. The crystallinity percentage of TOCNF recorded 73%.[42]. As a result of the oxidation reaction degrading amorphous regions, a greater proportion of these regions can now be found in the water-soluble fraction, leading to an increase in crystallinity.

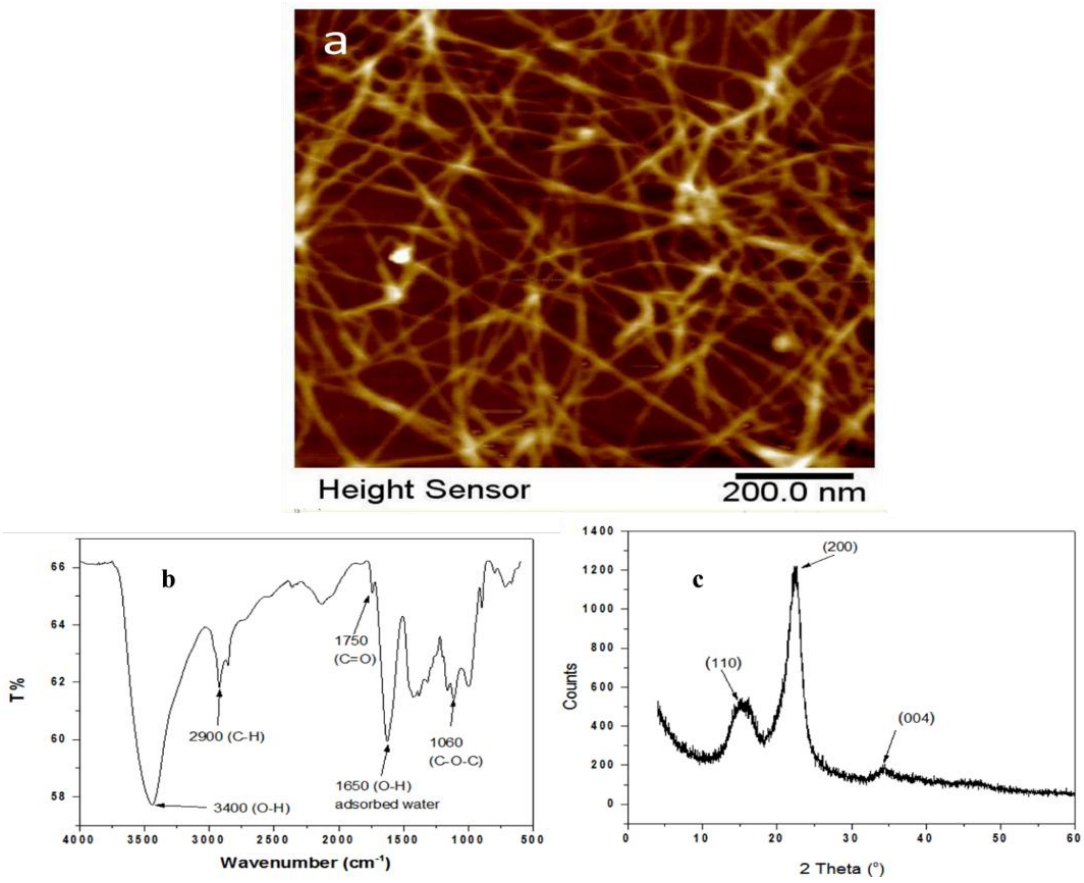

Figure 1. (a) AFM image (b) FT-IR spectrum, and (c) XRD pattern for TEMPO-CNFs.

3.2. Characterizations of TEMPO-CNF /Fe_3O_4 nanocomposite

The TEM image of the TEMPO-CNF/Fe_3O_4 nanocomposite showed that the Fe_3O_4 nanoparticles exhibit crystalline particles with spherical shapes, with diameter of 23 nm randomly distributed in the TEMPO-CNFs. Unique morphology with a smaller particle size might be due to the in-situ mineralization of Fe_3O_4 nanoparticles in the corporate of TEMPO-CNF. Moreover, TEMPO-CNF/Fe_3O_4 nanocomposite image showed uniformly dispersed Fe_3O_4 nanoparticles inside the oxidized fibers. The x-ray diffraction pattern of TEMPO-CNFs/Fe_3O_4 nanocomposite, shown in

figure 2 (b), exhibits the appearance of characteristic peaks at 2 theta = 30.3, 35.7, 43.4, and 63.2° relating to (2 2 0), (3 1 1), (4 0 0) and (4 4 0) planes respectively. These results were consistent with XRD for the standard Fe_3O_4 pattern (JCPDS, reference 01-075-0449) and indicate the cubic axial configuration of magnetite [43].

Figure 2 (b and d) FTIR spectrum of TEMPO-CNFs/Fe_3O_4 nanocomposite before and after adsorption respectively. The spectra showed bands at 3410, 2980, and 1750 cm^{-1} which assigned to the OH, C-H, and carbonyl groups, respectively. The absorption at 600 cm-1 represented to the Fe-O bond's absorption vibrations. Before and after MB adsorption, the TEMPO-CNF/Fe_3O_4 magnetite nanocomposite bands undergo significant modifications. In MB-loaded TEMPO-CNF/Fe_3O_4, characteristic bands are found at 1246 cm^{-1} (C-N stretching), 1487 cm-1 (N-H), and 1599 cm-1 (C=N of aromatic ring). These peaks prove that MB is absorbed by the TEMPO-CNF/Fe_3O_4. Additionally, the nanocomposite's characteristic bands expanded and shifted slightly. For instance, C=C stretching band shifted from 1620 to 1599 cm^{-1} and O-H stretching band shifted from 3400 to 3302 cm^{-1}. The hydrogen bonding and electrostatic interactions between the MB functional groups and the TEMPO-CNF/Fe_3O_4 are depicted in Scheme 1. These interactions are responsible for high adsorption capacity.

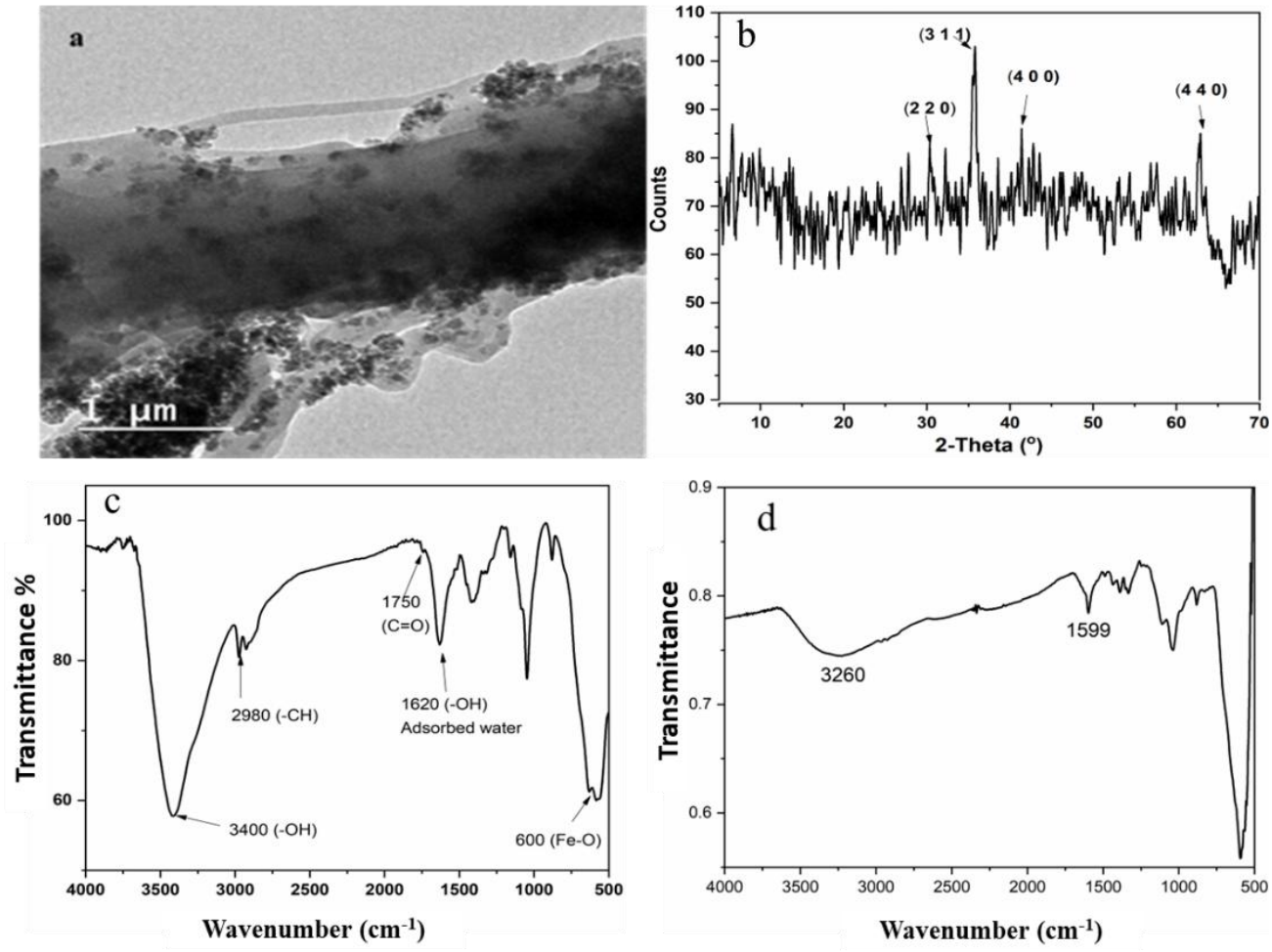

Figure 2. (a) Transmission electron microscope picture, (b) x-ray diffraction spectrum, (C) FT-IR for TEMPO-CNF/Fe_3O_4 nanocomposite and FT-IR spectrum of MB loaded nanocomposite (D).

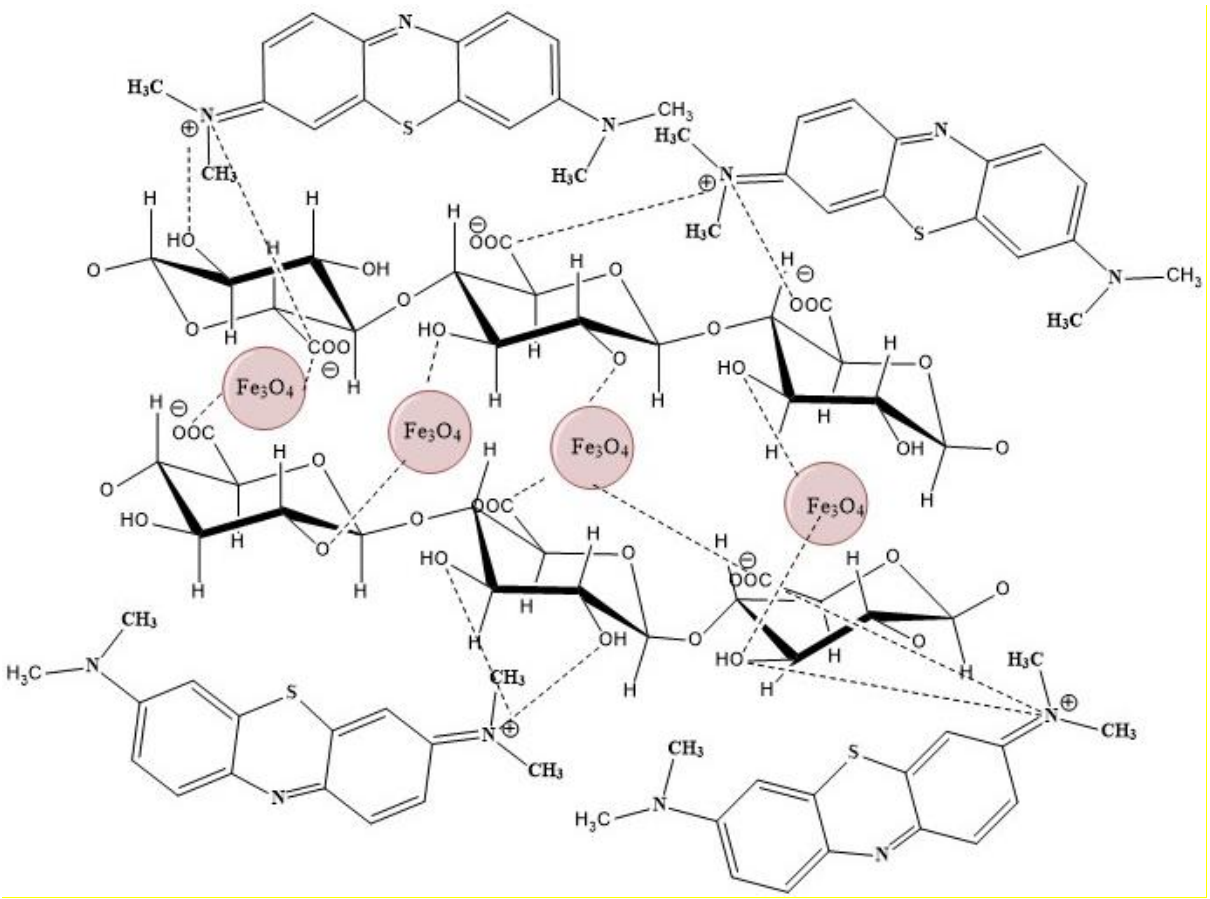

Scheme 1. The possible mechanism of MB adsorption onto TEMPO-CNF/Fe_3O_4

To determine the thermal stability of the produced sample, TGA was performed. TEMPO-CNF/Fe3O4 magnetite nanocomposite. Figure 3 shows the TGA curve of TEMPO-CNF and TEMPO-CNF/Fe_3O_4 nanocomposite. From 50 to 200 degrees Celsius, weight loss of 10.5% and 5.3% for TEMPO-CNF and TEMPO-CNF/Fe_3O_4 was obtained, respectively, owing to the release of the water absorbed contained on the interfaces of the two samples. The cellulose backbone in TEMPO-CNF decomposes at 230°C with a maximum weight loss at 350°C. The final weight loss of TEMPO-CNF equals 887%. The weight loss behavior of TEMPO-CNF/Fe_3O_4 magnetite nanocomposite was different from TEMPO-CNF The main weight loss was observed at 250 to 360 C corresponding to the decomposition of cellulose and the reaction of Fe_3O_4 with carbon which was the residue of the cellulose decomposition with the final weigh loss of 25%.

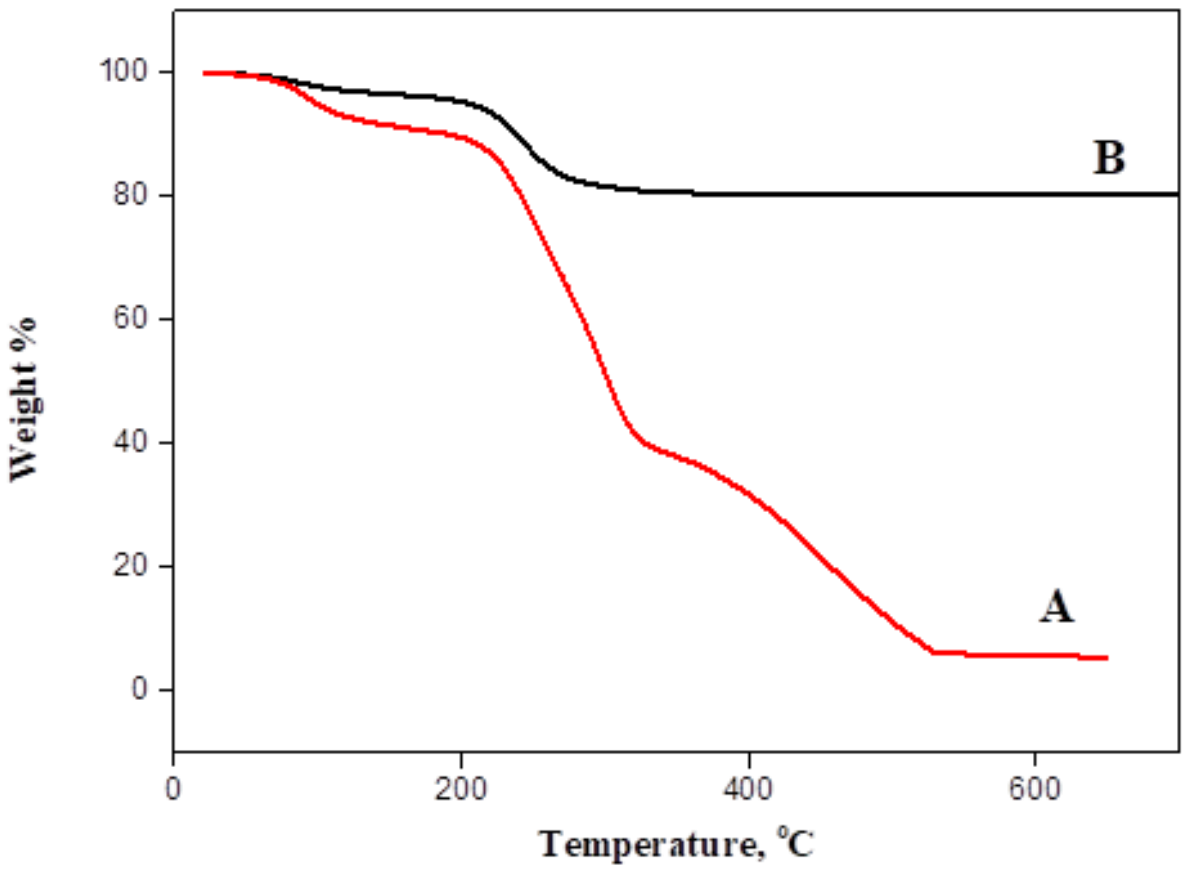

Figure 3: TGA of TEMPO-CNF and Fe_3O_4 composites (A) and (B) respectively

Using N2 adsorption-desorption isotherms, the textural characteristics of the synthesized nanocomposites were analyzed. The specific surface area was computed utilizing the Brunauer–Emmett–Teller (BET) formula, and the pore size distribution curves were acquired utilizing the Barrett–Joy–Halenda (BJH) method. Figure 4 illustrates the N2 adsorption-desorption isotherms of nanocomposites. The measured surface area of the TEMPO-CNF/Fe_3O_4 nanocomposite was 64.7 m2/g. The increased BET surface area of the TEMPO-CNF/Fe_3O_4 nanocomposite compared to CNF was attributable to the inclusion of TEMPO-CNF and Fe_3O_4 nanoparticles in the materials; consequently, the nanocomposite provided better access and most commonly adsorption sites. In addition, the nanocomposites' pore sizes were mainly distributed in the 12 nm range, attributed to the presence of mesopores in the materials. Consequently, these results revealed that TEMPO-CNF/Fe_3O_4 nanocomposite exhibited a more porous structure, which was

suitable towards the diffusion of the adsorbate.

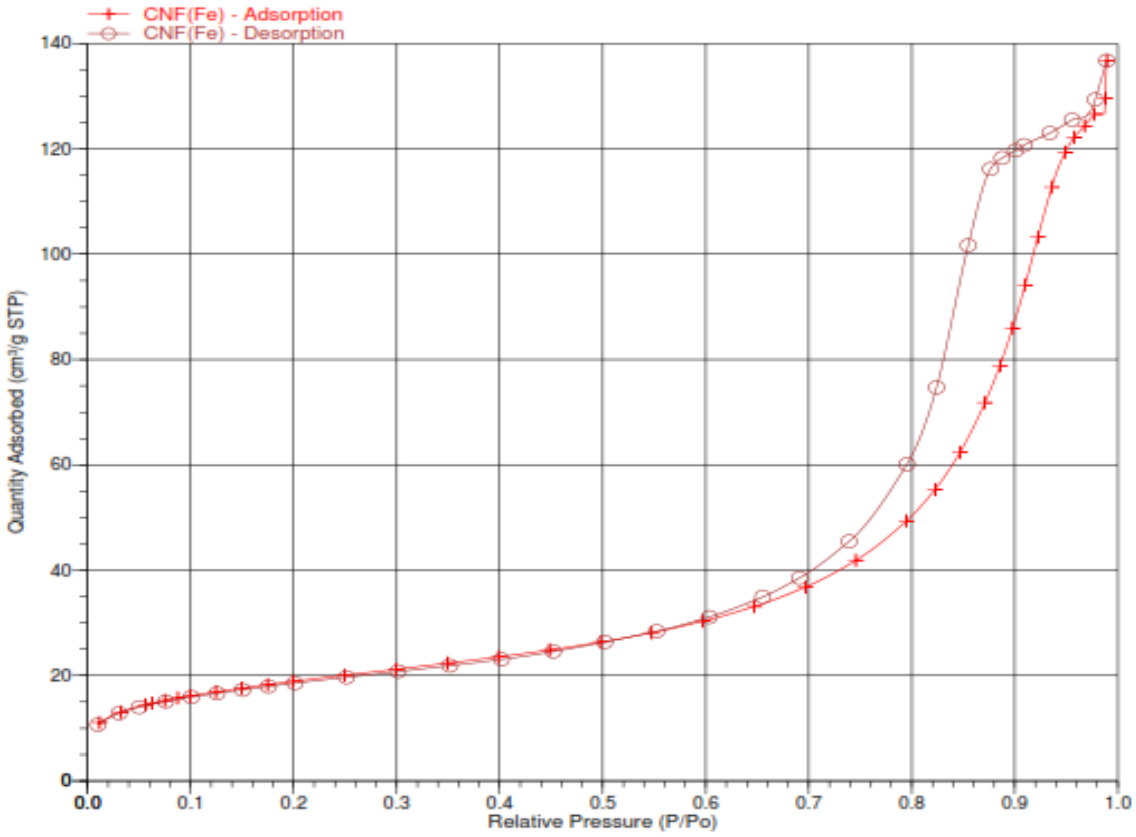

Figure 4. N_2 adsorption−desorption isotherms of TEMPO-CNF/Fe_3O_4 nanocomposite

Figure 5 illustrates the SEM study of TEMPO-CNF and TEMPO-CNF/Fe_3O_4 nanocomposite morphology. Different fiber widths are displayed in TEMPO-CNF. Furthermore, the TEMPO-CNF/Fe_3O_4 nanocomposite had a sphere shape with an approximate diameter of less than 10 nm. However, the SEM image indicates that the nanocomposite displays aggregation because Fe_3O_4 is homogenously mixed with TEMPO-CNF. However, the SEM image signifies that the nanocomposite displays aggregation because of Fe_3O_4 homogenously mixed with TEMPO-CNF. Additionally, Fe_3O_4 nanoparticles seem to be more distinctive and consistent. This is probably because of TEMPO-CNF and Fe_3O_4 nanoparticles interact together decreases the forces that make Fe_3O_4 nanoparticles preventing them from sticking together. After loading with MB, SEM images exhibited denser surface and EDX spectra prove the MB adsorption due to the appearance of characteristic peaks for Nitrogen and Sulphur.

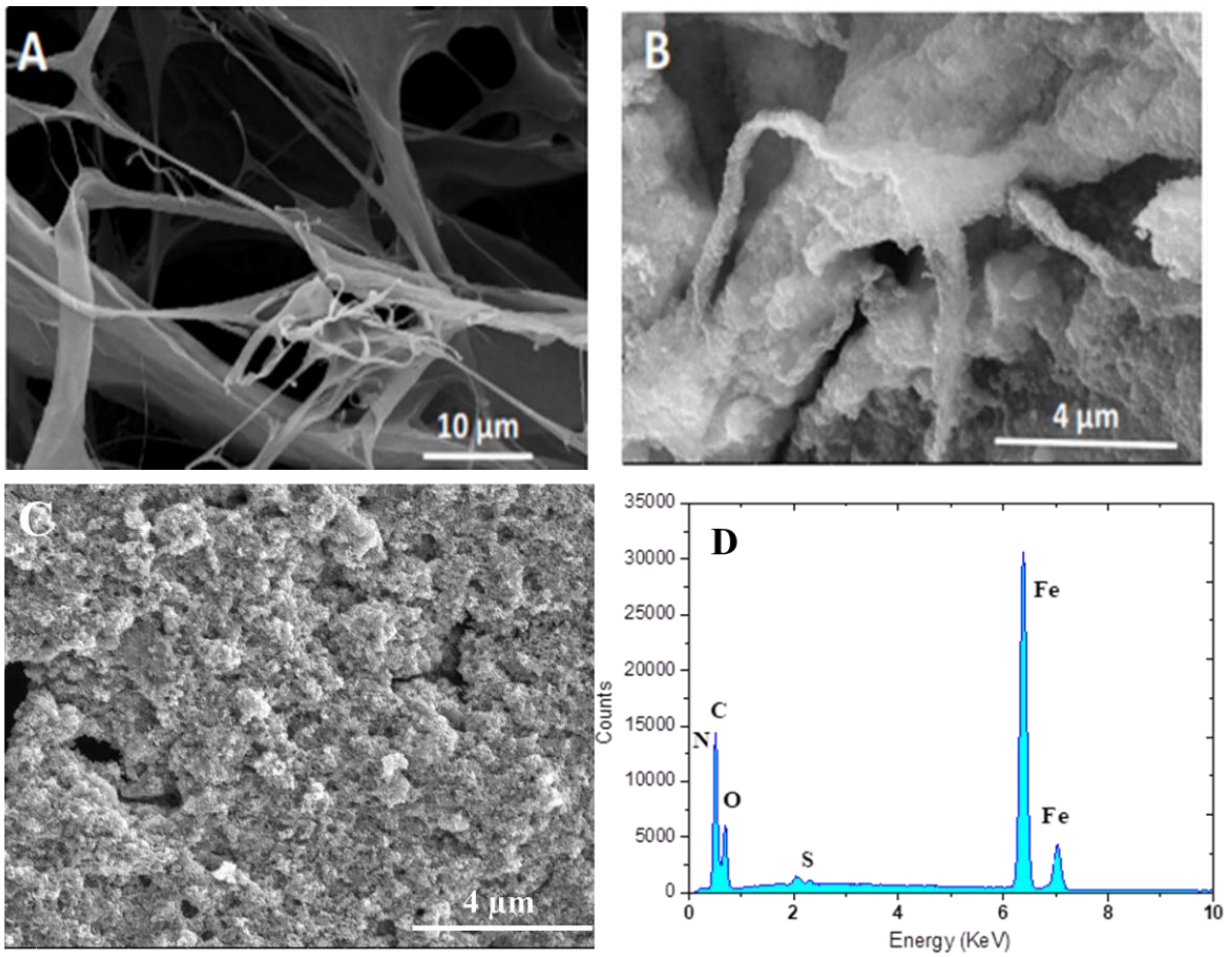

Figure 5. SEM images of TEMPO-CNF (A), TEMPO-CNF/Fe_3O_4 before (B) and after (C) MB adsorption, and EDX of TEMPO-CNF/Fe_3O_4 nanocomposite loaded MB (D).

3.2. MB absorption using TEMPO-CNF/Fe_3O_4 nanocomposite.

The obtained TEMPO-CNF/Fe_3O_4 nanocomposite was subjected to organic dye removal from effluent. To better understand the behavior of the current nanocomposite, using TEMPO-CNF/Fe_3O_4 as an adsorbent, various factors such as pH, contact time, and dye concentration were investigated.

3.2.1. Effect of pH

Figure 6 illustrates the influence of pH on the absorption rate of TEMPO-CNF/Fe_3O_4 nanocomposite. The results demonstrate that the adsorption of MB increased slightly to achieve the optimal value of 79.5 mg/g at pH 7. At a low pH, TEMPO-CNF/Fe_3O_4 functional groups were protonated and showed as positive charge groups. Electrostatic repulsive force for both MB

and protonated groups may inhibit uptake [44]. This demonstrated the function of Fe_3O_4 nanoparticles in enhancing the adsorption performance of the prepared nanocomposites, which possesses extra sites for ionic attraction with cationic dye. The pH study suggests that the adsorption efficiency of the TEMPO-CNF/Fe_3O_4 nanocomposite is improved in neutral conditions. Increasing the capability of adsorption of cationic dyes with pH has been recorded in previous work [45].

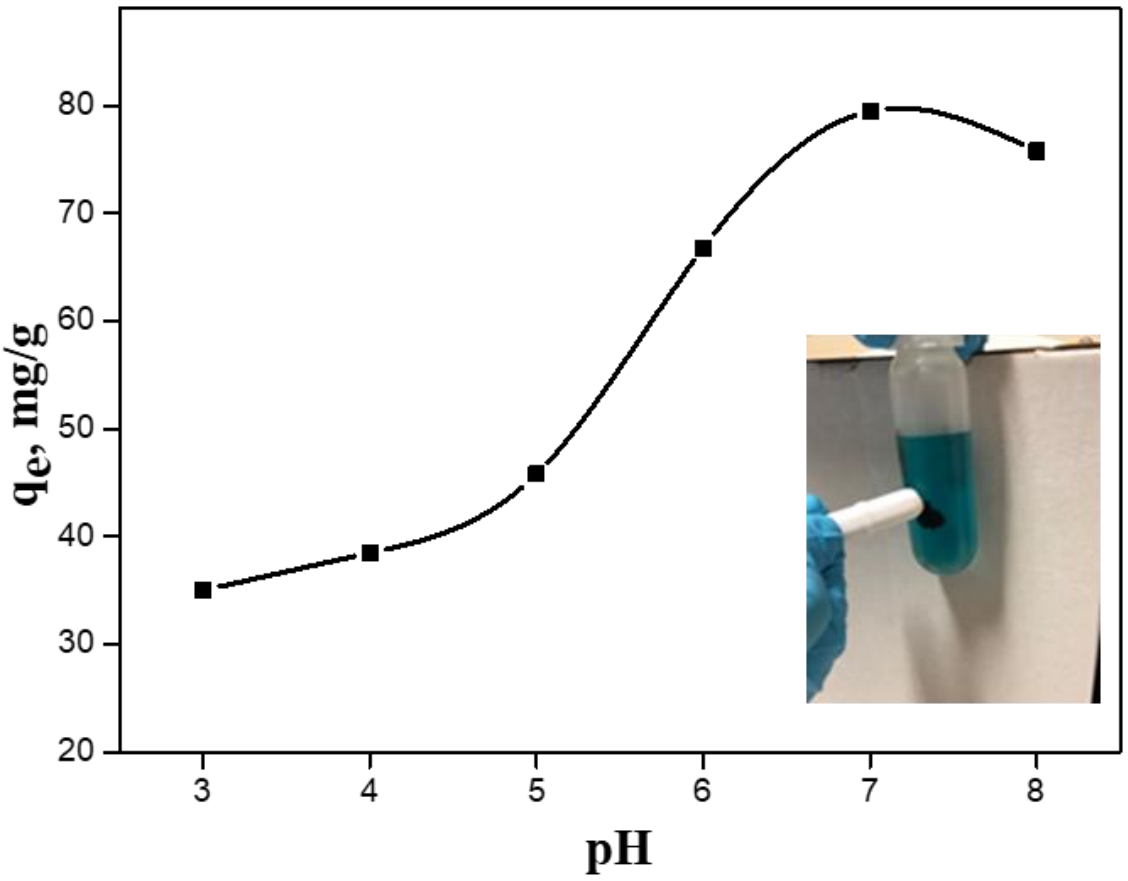

Figure 6: Influence of different pH on the MB adsorption capability of nanocomposite TEMPO-CNF Fe_3O_4.

3.2.2. Effect of contact time and adsorption kinetics.

The rate of MB adsorption is dependent on the amount of time that TEMPO-CNF/Fe_3O_4 nanocomposite is in touch with the dye solution. The adsorption of MB on TEMPO-CNF/Fe_3O_4

nanocomposite presents a trend of rapid increase through the first 90 minutes and then reaches equilibrium after 120 minutes as displayed in figure 7.

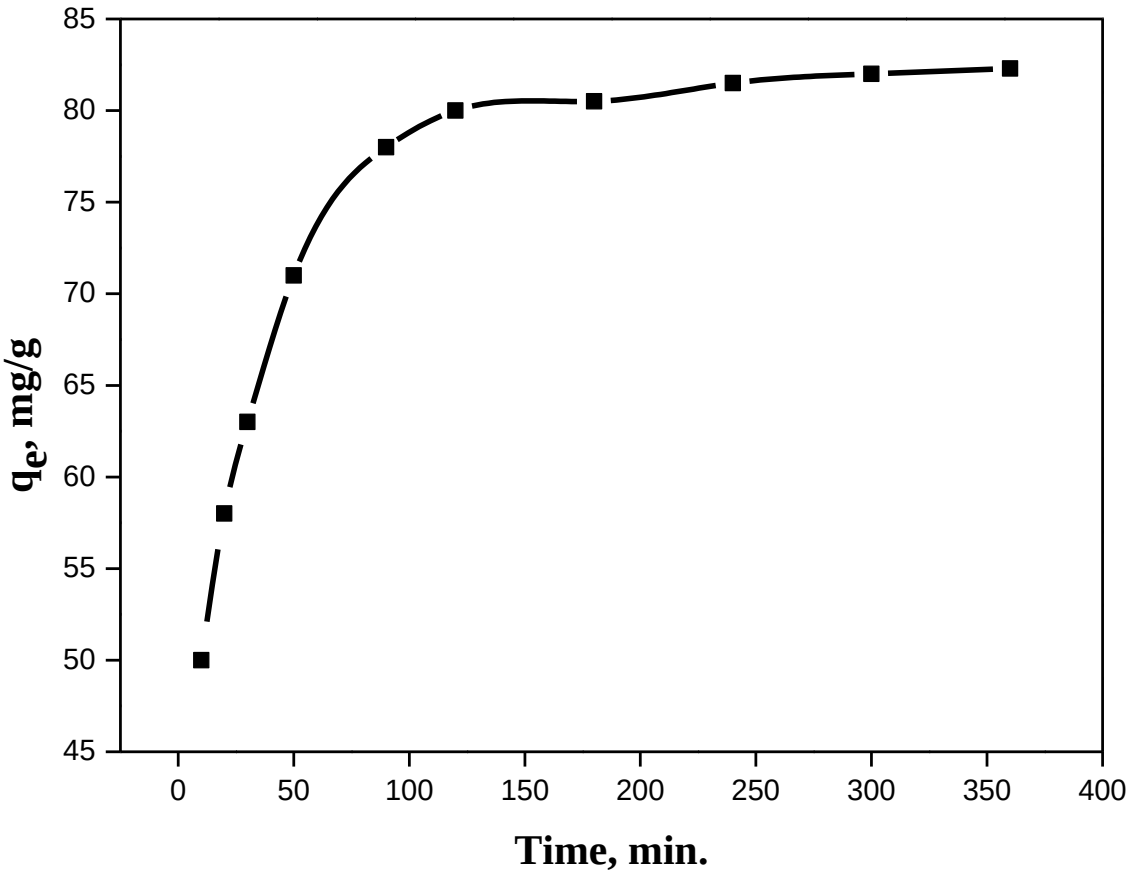

Figure 7: Effect of time on the adsorption of TEMPO-CNF/Fe_3O_4 nanocomposite and the pseudo-second-order kinetic model that was applied.

In formulae 1 and 2, the pseudo-first- and -second-order models are illustrated, respectively.

$$Log\ (q_e - q_t) = Log(q_e) - \frac{K_1}{2.303}\ t \qquad (1)$$

$$\frac{t}{q_t} = \frac{t}{q_e} + \frac{1}{K_2 {q_e}^2} \qquad (2)$$

Table 1 illustrates the characteristics of TEMPO-CNF/Fe3O4 kinetic. In the case of the 1st order, the coefficient of determination is relatively low, and the calculated qe is far from the experimental one. From pseudo second order models, the coefficient of determination (R2) is nearly 0.99, and the calculated qe (87.7 mg/g) is close to the experimental qe (82.3 mg/g). This

signifies that the kinetic data were better fitted with the pseudo-second-order model. The pseudo-second-order kinetic model assumes that the rate-limiting process is chemisorption-related. This chemisorption assumption based on the kinetics result will be confronted with the enthalpic data.

Table 1. Kinetic characteristics for MB adsorption by nanocomposite TEMPO-CNF/Fe_3O_4

Pseudo first order-model				Pseudo second- order model		
$q_{e,\ exp}$	$q_{e,\ cal}$	K_1	R^2	$q_{e,\ cal}$	K_2	R^2
(mg g^{-1})	(mg g^{-1})	(min^{-1})		(mg g^{-1})	(g $mg^{-1}min^{-1}$)	
82.3	69	0.0032	0.63	84.7	$1.47 * 10^{-3}$	0.99

3.2.3. Effect of MB concentration and equilibrium isotherm.

Figure 8 illustrates the adsorption characteristics of TEMPO-CNF/Fe_3O_4 at different MB concentrations. The maximum rate of MB removal is 234 mg/g at a concentration of 300 ppm. Higher concentrations tend to level off the adsorption ability.

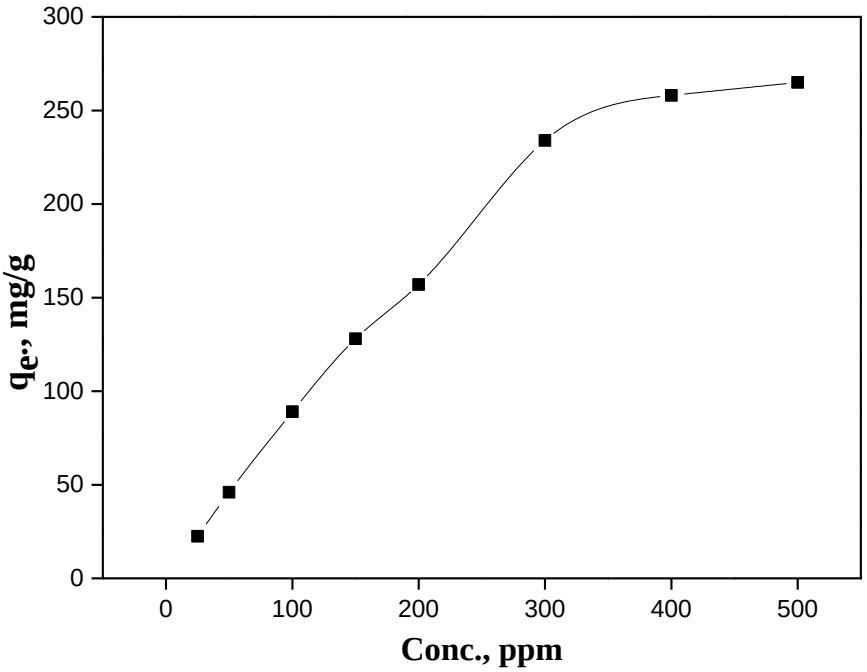

Figure 8: Influence of initial Concentrations on TEMPO-CNF/Fe_3O_4 nanocomposite adsorption capability. Experiments on adsorption: sample dose: 0.05 g/50 mL; pH: 7.0; interaction time: 24 hours.

To get more precise information on the sorption process, the Langmuir and the Freundlich isotherm models have been applied. In the case of the Langmuir model, the parameters were calculated from equation (3) [46].

$$\frac{C_e}{q_e} = \frac{1}{K_L Q_{max}} + \frac{C_e}{Q_{max}} \qquad (3)$$

with Q_{max} and C_e maximum adsorption capacity and equilibrium concentration respectively, and K_L is the Langmuir constant. The Freundlich model is represented in equation 4:

$$\log(q_e) = \log K_F + \left(\frac{1}{n}\right).logC_e \qquad (4)$$

The Freundlich constants K_F and 1/n, respectively, represent the adsorption capacity and adsorption intensity.

The calculated correlation coefficients for both models are displayed in Table 2. High correlation coefficients (R2 > 0.992) have been found for the Langmuir model, while the Freundlich model revealed low linear coefficient values (0.91). In addition, the values of KF and n factors for TEMPO-CNF/Fe_3O_4 nanocomposite are 30 and 1.92. These calculations indicated that this model does not right method for MB adsorption onto the produced nanocomposite. This indicates that the Langmuir equation is consistent with the MB absorption on the TEMPO-CNF/Fe_3O_4 nanocomposite. This demonstrates that monolayer adsorption of MB happened on the nanocomposite. The findings indicated that the parameter qmax was 303 mg/g.

Table 2. Different equilibrium models for TEMPO-CNF/Fe_3O_4 nanocomposite MB absorption parameters.

Langmuir isotherm constants			Freundlich isotherm constants		
K_L (L mg^{-1})	qm (mg g^{-1})	R^2	P (mg L^{-1})	n	R^2
0.037	303	0.992	30	1.92	0.91

In table 3, a comparison is made between TEMPO-CNF/Fe_3O_4 nanocomposites as well as other adsorbents for MB absorption. TEMPO-CNF/Fe_3O_4 nanocomposite had greater MB absorption than other cellulosic materials described in prior studies.

Table 3. The Highest MB adsorption capacities of common cellulose products.

Adsorbent	Maximum adsorption of MB (mg/g)	References
TEMPO-oxidized cellulose beads	495	[47]
Graphene oxide/cellulose strands	480.8	[48]
Hybrid of cellulose-grafted SPI and hydroxyapatite	454	[2]
Our nanocomposite	303	This work
Alginate/cellulose nanocrystals	256.4	[49]
Carboxymethyl cellulose/graphene composite	222.7	[50]
Calcium phosphate and carboxymethyl cellulose-g-polymethacrylic acid	180.2	[45]
Humic acid/graphene oxide	55	[51]

3.2.4. Desorption and regeneration studies

The TEMPO-CNF/Fe_3O_4 showed good performance in recycling treatment with MB dye. The pH study showed that TEMPO-CNF/Fe_3O_4 did not significantly adsorb MB at pH < 3.0, which indicates that the adsorbed MB could be desorbed in solution with such pH values. Moreover, MB dissolved easily in organic solvents and consequently desorption of MB dye was carried out with mixture of 5% (v/v) acetic acid and methanol. The results of adsorption efficiency of the examined TEMPO-CNF/Fe_3O_4 after five cycles are shown in figure 9. The nanocomposite maintains around 67 of its original efficiency by the end of the fifth regeneration cycle.

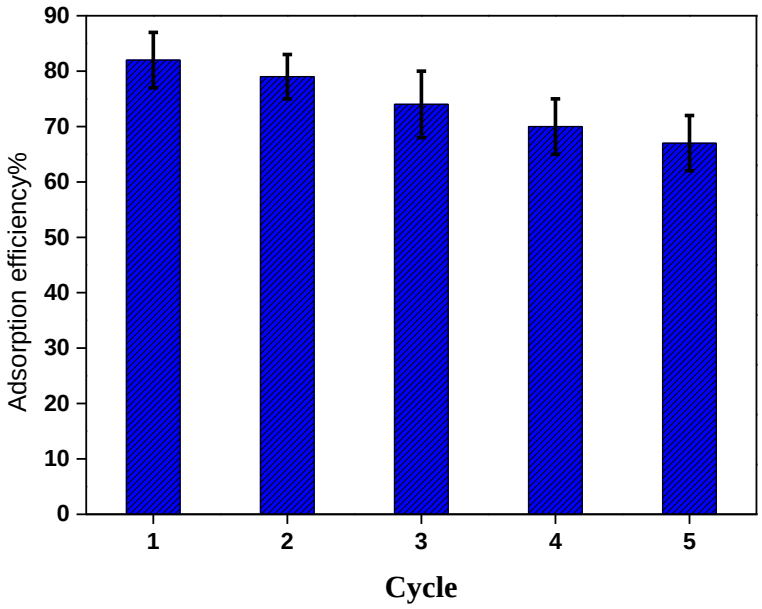

Figure 9: Adsorption–desorption cycles of MB for TEMPO-CNF/Fe_3O_4 nanocomposite.

3.2.5. Isothermal titration calorimetry

Isothermal titration calorimetry was performed to study the energy of interaction produced when MB is placed in contact with the nanocomposite. Figure 10 shows the results of the ITC experiment using a 10 mM MB solution on TEMPO-CNF/Fe_3O_4 together with a comparison of the dilution effect in the absence of powder in the cell. The shape of the heat flow is similar for the two systems. The signal is intense for the first injections, and then gradually decreases with an increasing number of injections. This indicates a regular decrease in the endothermic behavior until stabilization. The difference between adsorption and dilution is observed from the intensities of the peaks, with for example for the 1st peak, -2.8 µW, and -4.1 µW respectively. This indicates that the heat effect is slightly endothermic after subtraction of the dilution effect.

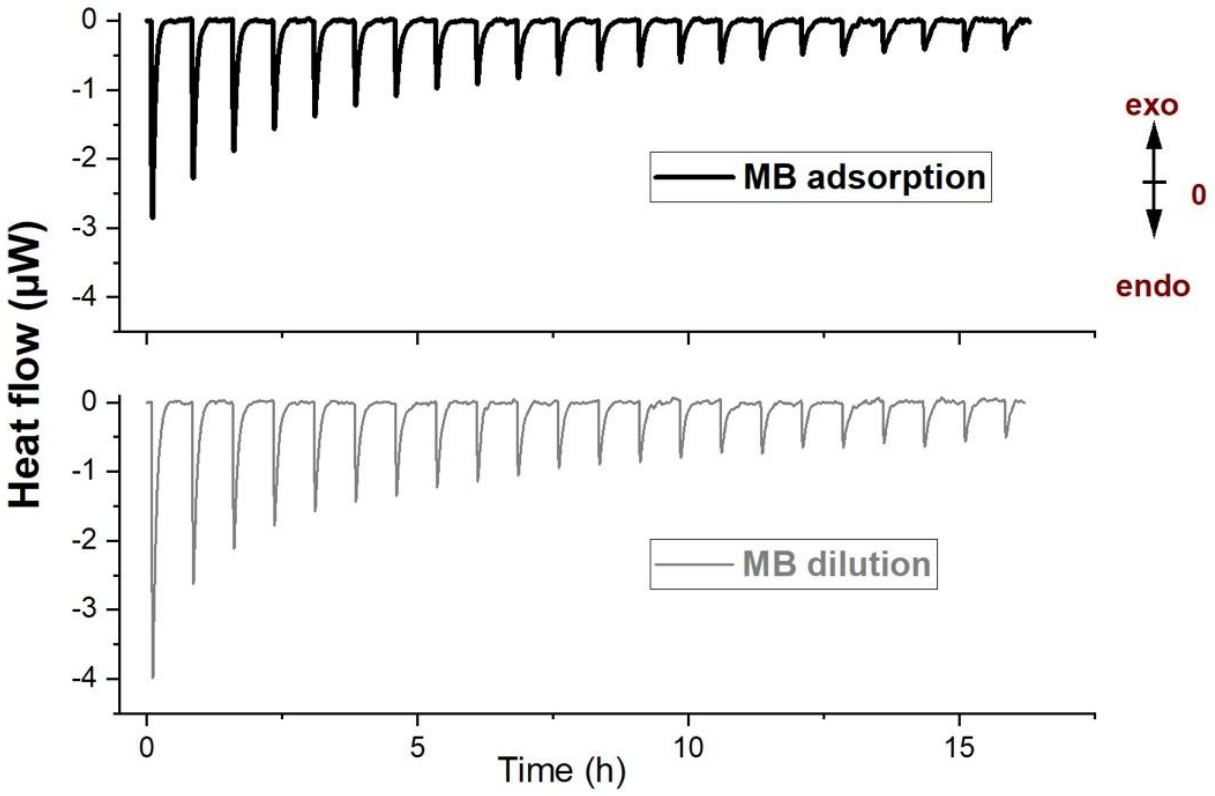

Figure 10. Thermogram of the ITC measurements of the sorption of MB on TEMPO-CNF/Fe_3O_4 nanocomposite in water performed with an initial concentration of 10 mM for the stock solution of MB (black curve measurement with nanocomposite) and the grey curve represents the dilution of MB (measurement without nanocomposite).

The enthalpic contribution has been calculated from the integration of the heat response obtained from the raw ITC data. The sorption enthalpy describes the evolution of the interactions during the loading. Cumulative displacement enthalpy (∑ΔHdpl) may be plotted in function of the adsorbed amount obtained from the adsorption isotherms as displayed in Figure 11. For low coverage and before surface saturation, the ITC shows a linear evolution of the interaction process. Then, when the maximum capacity is almost reached, the enthalpy levels off. The cumulative enthalpy of displacement ∑ΔHdpl or ΔdplHcum was estimated on the initial portion of the adsorption isotherm. ΔdplHcum is estimated at 5.2 kJ/mol and the positive value of ΔH indicated that the adsorption process was endothermic and spontaneous. The obtained value is rather small, and means that the enthalpic contribution is weak. The comparison with other studies is rather tricky. Indeed, in these studies the enthalpic contribution ΔH is classically

calculated from Van't Hoff equation with isotherm data acquired at various temperatures up to 45 °C. In studies on MB sorption thermodynamics [48,51], the enthalpy is in the range of 18-22.5 kJ/mol, higher than the present work. Nevertheless, in our case, it seems that our Langmuir constant is higher, which is in line with the pseudo second order describe before, and this could explain the observed differences, in correlation with the entropic contribution.

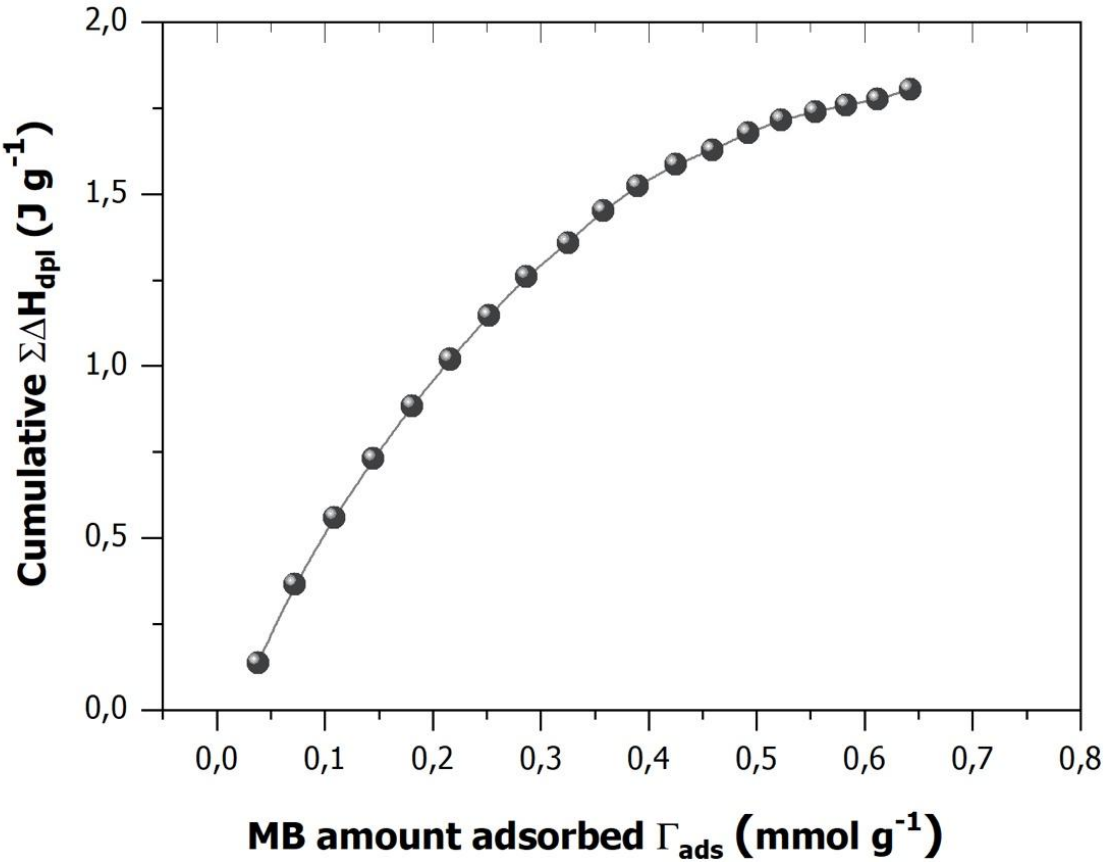

Figure 11: Cumulative displacement enthalpy versus the adsorbed amount for adsorption in the water of MB on TEMPO-CNF/Fe_3O_4 nanocomposite.

4. Conclusion

Tempo-oxidized cellulose nanofiber/magnetite composite (TEMPO-CNF/Fe_3O_4) was prepared through the co-precipitation technique as a versatile adsorbent for the removal of MB from wastewater. TEM observation exhibited the successfully preparation of cellulose nanofiber with a diameter ranged from 10-15 nm and homogenous spherical magnetic nanoparticles (Fe_3O_4) were immobilized. A pseudo-second order and Langmuir isotherm with an adsorption capacity of 303 mg/g and a weak interaction enthalpy define MB adsorption onto TEMPO-CNF/Fe_3O_4.

This study provides an alternative bio-nanocomposite adsorbent, TEMPO-CNF/Fe_3O_4, with effective organic pollutant adsorption capacity.

Availability of data and materials

The research data associated with a paper is available.

Conflict of interest:

The authors declare no conflict of interest.

Ethical statement

In the manuscript, the authors stated that no informed consent was obtained for animal or human experiments.

Author Contributions:

Ahmed Salama and Benedicte Prelot shared equally in funding acquisition and project administration. A.S., B.P., R. A., M. D., M. A. investigation, methodology, validation, and writing—original draft. P. H. methodology, writing—review and editing. All authors have read and agreed to the submitted version of the manuscript.

Acknowledgement

The authors would like to thank the Academy of Scientific Research and Technology, Egypt, for providing financial support for the study efforts through the Egypt-France Scientific and Technological Cooperation Program PHC "IMHOTEP" 41898XD..

References

[1] P. Wang, T. Yan, L. Wang, Removal of congo red from aqueous solution using magnetic chitosan composite microparticles, BioResources. 8 (2013) 6026–6043. https://doi.org/10.15376/biores.8.4.6026-6043.

[2] A. Salama, New sustainable hybrid material as adsorbent for dye removal from aqueous solutions, J. Colloid Interface Sci. 487 (2017) 348–353. https://doi.org/10.1016/j.jcis.2016.10.034.

[3] H. Qian, J. Wang, L. Yan, Synthesis of lignin-poly(N-methylaniline)-reduced graphene oxide hydrogel for organic dye and lead ions removal, J. Bioresour. Bioprod. 5 (2020) 204–210. https://doi.org/10.1016/j.jobab.2020.07.006.

[4] J. Jjagwe, P.W. Olupot, E. Menya, H.M. Kalibbala, Synthesis and Application of Granular Activated Carbon from Biomass Waste Materials for Water Treatment: A Review, J.

Bioresour. Bioprod. 6 (2021) 292–322. https://doi.org/10.1016/j.jobab.2021.03.003.

[5] G. Darmograi, B. Prelot, A. Geneste, L.-C. De Menorval, J. Zajac, Removal of three anionic orange-type dyes and Cr(VI) oxyanion from aqueous solutions onto strongly basic anion-exchange resin. The effect of single-component and competitive adsorption, Colloids Surfaces A Physicochem. Eng. Asp. 508 (2016) 240–250. https://doi.org/10.1016/j.colsurfa.2016.08.063.

[6] G. Darmograi, M. Kus, G. Martin-Gassin, J. Zajac, S. Cavaliere, B. Prelot, How competitive species such as buffer solutions influence the adsorption of dyes onto photocatalyst TiO 2 particles, Mater. Res. Bull. 94 (2017) 70–76. https://doi.org/10.1016/j.materresbull.2017.05.025.

[7] G. Darmograi, B. Prelot, G. Layrac, D. Tichit, G. Martin-Gassin, F. Salles, J. Zajac, Study of Adsorption and Intercalation of Orange-Type Dyes into Mg–Al Layered Double Hydroxide, J. Phys. Chem. C. 119 (2015) 23388–23397. https://doi.org/10.1021/acs.jpcc.5b05510.

[8] G. Darmograi, B. Prelot, A. Geneste, G. Martin-Gassin, F. Salles, J. Zajac, How Does Competition between Anionic Pollutants Affect Adsorption onto Mg–Al Layered Double Hydroxide? Three Competition Schemes, J. Phys. Chem. C. 120 (2016) 10410–10418. https://doi.org/10.1021/acs.jpcc.6b01888.

[9] A. Salama, P. Hesemann, New N-guanidinium chitosan/silica ionic microhybrids as efficient adsorbent for dye removal from waste water, Int. J. Biol. Macromol. 111 (2018) 762–768. https://doi.org/10.1016/j.ijbiomac.2018.01.049.

[10] H. Hassan, A. Salama, A.K. El-ziaty, M. El-Sakhawy, New chitosan/silica/zinc oxide nanocomposite as adsorbent for dye removal, Int. J. Biol. Macromol. 131 (2019) 520–526. https://doi.org/10.1016/j.ijbiomac.2019.03.087.

[11] A. Salama, R.E. Abou-Zeid, Ionic chitosan/silica nanocomposite as efficient adsorbent for organic dyes, Int. J. Biol. Macromol. 188 (2021) 404–410. https://doi.org/10.1016/j.ijbiomac.2021.08.021.

[12] J. Zheng, B. Yan, L. Feng, Q. Zhang, C. Zhang, W. Yang, J. Han, S. Jiang, S. He, Potassium citrate assisted synthesis of hierarchical porous carbon materials for high performance supercapacitors, Diam. Relat. Mater. 128 (2022) 109247. https://doi.org/10.1016/j.diamond.2022.109247.

[13] R.E. Abou-Zeid, K.H. Kamal, M.E. Abd El-Aziz, S.M. Morsi, S. Kamel, Grafted TEMPO-oxidized cellulose nanofiber embedded with modified magnetite for effective adsorption of lead ions, Int. J. Biol. Macromol. 167 (2021) 1091–1101. https://doi.org/10.1016/j.ijbiomac.2020.11.063.

[14] E. Bagheri, H. Rahnama, M.A. Hassannia, T. Behzad, P. Mosaddegh, Oriented polylactic acid/graphene oxide nanocomposites with high mechanical and thermal properties, J. Thermoplast. Compos. Mater. 54 (2021) 089270572110386. https://doi.org/10.1177/08927057211038625.

[15] A. Salama, S. Etri, S.A.A. Mohamed, M. El-Sakhawy, Carboxymethyl cellulose prepared from mesquite tree: New source for promising nanocomposite materials, Carbohydr. Polym. 189 (2018) 138–144. https://doi.org/10.1016/j.carbpol.2018.02.016.

[16] A. Salama, Preparation of CMC-g-P(SPMA) super adsorbent hydrogels: Exploring their capacity for MB removal from waste water, Int. J. Biol. Macromol. 106 (2018) 940–946. https://doi.org/10.1016/j.ijbiomac.2017.08.097.

[17] R.E. Abouzeid, A. Salama, E.M. El-Fakharany, V. Guarino, Mineralized Polyvinyl Alcohol/Sodium Alginate Hydrogels Incorporating Cellulose Nanofibrils for Bone and Wound Healing, Molecules. 27 (2022) 697. https://doi.org/10.3390/molecules27030697.

[18] M.L. Hassan, R.E.A. Zeid, S.M. Fadel, M. El Sakhawy, R. Khiari, Cellulose nanocrystals and carboxymethyl cellulose from olive stones and their use to improve paper sheets properties, Int. J. Nanoparticles. 7 (2014) 261. https://doi.org/10.1504/IJNP.2014.067613.

[19] R.E. Abouzeid, R. Khiari, N. El-Wakil, A. Dufresne, Current State and New Trends in the Use of Cellulose Nanomaterials for Wastewater Treatment, Biomacromolecules. 20 (2019) 573–597. https://doi.org/10.1021/acs.biomac.8b00839.

[20] A. Salama, P. Hesemann, Recent Trends in Elaboration, Processing, and Derivatization of Cellulosic Materials Using Ionic Liquids, ACS Sustain. Chem. Eng. 8 (2020) 17893–17907. https://doi.org/10.1021/acssuschemeng.0c06913.

[21] N.S. El-Sayed, A. Salama, V. Guarino, Coupling of 3-Aminopropyl Sulfonic Acid to Cellulose Nanofibers for Efficient Removal of Cationic Dyes, Materials (Basel). 15 (2022) 6964. https://doi.org/10.3390/ma15196964.

[22] S. Hokkanen, A. Bhatnagar, M. Sillanpää, A review on modification methods to cellulose-based adsorbents to improve adsorption capacity, Water Res. 91 (2016) 156–173. https://doi.org/10.1016/j.watres.2016.01.008.

[23] R.E. Abouzeid, R. Khiari, A. Salama, M. Diab, D. Beneventi, A. Dufresne, In situ mineralization of nano-hydroxyapatite on bifunctional cellulose nanofiber/polyvinyl alcohol/sodium alginate hydrogel using 3D printing, Int. J. Biol. Macromol. 160 (2020) 538–547. https://doi.org/10.1016/j.ijbiomac.2020.05.181.

[24] M. Shayan, J. Gwon, M.S. Koo, D. Lee, A. Adhikari, Q. Wu, pH-responsive cellulose nanomaterial films containing anthocyanins for intelligent and active food packaging, Cellulose. 1 (2022). https://doi.org/10.1007/s10570-022-04855-5.

[25] A. El-Gendy, R.E. Abou-Zeid, A. Salama, M.A. Diab, M. El-Sakhawy, TEMPO-oxidized cellulose nanofibers/polylactic acid/TiO2 as antibacterial bionanocomposite for active packaging, Egypt. J. Chem. 60 (2017) 1007–1014. https://doi.org/10.21608/ejchem.2017.1835.1153.

[26] D. Jaspal, A. Malviya, Composites for wastewater purification: A review, Chemosphere. 246 (2020) 125788. https://doi.org/10.1016/j.chemosphere.2019.125788.

[27] M.A. Dutt, M.A. Hanif, F. Nadeem, H.N. Bhatti, A review of advances in engineered

composite materials popular for wastewater treatment, J. Environ. Chem. Eng. 8 (2020) 104073. https://doi.org/10.1016/j.jece.2020.104073.

[28] B. Yan, J. Zheng, L. Feng, C. Du, S. Jian, W. Yang, Y.A. Wu, S. Jiang, S. He, W. Chen, Wood-derived biochar as thick electrodes for high-rate performance supercapacitors, Biochar. 4 (2022) 50. https://doi.org/10.1007/s42773-022-00176-9.

[29] A.M. Gutierrez, T.D. Dziubla, J.Z. Hilt, Recent advances on iron oxide magnetic nanoparticles as sorbents of organic pollutants in water and wastewater treatment, Rev. Environ. Health. 32 (2017) 111–117. https://doi.org/10.1515/reveh-2016-0063.

[30] A.M. El-Nahas, T.A. Salaheldin, T. Zaki, H.H. El-Maghrabi, A.M. Marie, S.M. Morsy, N.K. Allam, Functionalized cellulose-magnetite nanocomposite catalysts for efficient biodiesel production, Chem. Eng. J. 322 (2017) 167–180. https://doi.org/10.1016/j.cej.2017.04.031.

[31] R.E. Abouzeid, R. Khiari, K.A. Ali, Activated Charcoal/Alginate Nanocomposite Beads for Efficient Adsorption of the Cationic Dye Methylene Blue: Kinetics and Equilibrium, Chem. Africa. (2022). https://doi.org/10.1007/s42250-022-00560-9.

[32] O. V. Alekseeva, A.N. Rodionova, N.A. Bagrovskaya, A. V. Agafonov, A. V. Noskov, Hydroxyethyl cellulose/bentonite/magnetite hybrid materials: structure, physicochemical properties, and antifungal activity, Cellulose. 24 (2017) 1825–1836. https://doi.org/10.1007/s10570-017-1212-2.

[33] P. Kanmani, J. Aravind, M. Kamaraj, P. Sureshbabu, S. Karthikeyan, Environmental applications of chitosan and cellulosic biopolymers: A comprehensive outlook, Bioresour. Technol. 242 (2017) 295–303. https://doi.org/10.1016/j.biortech.2017.03.119.

[34] G.A. Kloster, N.E. Marcovich, M.A. Mosiewicki, Composite films based on chitosan and nanomagnetite, Eur. Polym. J. 66 (2015) 386–396. https://doi.org/10.1016/j.eurpolymj.2015.02.042.

[35] R.E. Morsi, A.M. Al-Sabagh, Y.M. Moustafa, S.G. ElKholy, M.S. Sayed, Polythiophene modified chitosan/magnetite nanocomposites for heavy metals and selective mercury removal, Egypt. J. Pet. 27 (2018) 1077–1085. https://doi.org/10.1016/j.ejpe.2018.03.004.

[36] O. Bezdorozhev, T. Kolodiazhnyi, O. Vasylkiv, Precipitation synthesis and magnetic properties of self-assembled magnetite-chitosan nanostructures, J. Magn. Magn. Mater. 428 (2017) 406–411. https://doi.org/10.1016/j.jmmm.2016.12.048.

[37] N. Singh, S. Yadav, S.K. Mehta, A. Dan, In situ incorporation of magnetic nanoparticles within the carboxymethyl cellulose hydrogels enables dye removal, J. Macromol. Sci. Part A. 59 (2022) 271–284. https://doi.org/10.1080/10601325.2022.2026788.

[38] A. Salama, R.E. Abou-Zeid, I. Cruz-Maya, V. Guarino, Soy protein hydrolysate grafted cellulose nanofibrils with bioactive signals for bone repair and regeneration, Carbohydr. Polym. 229 (2020). https://doi.org/10.1016/j.carbpol.2019.115472.

[39] F.-T. J.Ngenefeme, N. J. Eko, Y. D. Mbom, N. D. Tantoh, K.W. M. Rui, A One Pot Green

Synthesis and Characterisation of Iron Oxide-Pectin Hybrid Nanocomposite, Open J. Compos. Mater. 03 (2013) 30–37. https://doi.org/10.4236/ojcm.2013.32005.

[40] J.J. Zajac, Calorimetry at the Solid–Liquid Interface, in: 2013: pp. 197–270. https://doi.org/10.1007/978-3-642-11954-5_6.

[41] B. Yan, J. Zheng, L. Feng, W. Chen, W. Yang, Y. Dong, S. Jiang, Q. Zhang, S. He, All-cellulose-based high-rate performance solid-state supercapacitor enabled by nitrogen doping and porosity tuning, Diam. Relat. Mater. 128 (2022) 109238. https://doi.org/10.1016/j.diamond.2022.109238.

[42] L. Segal, J.J. Creely, A.E. Martin, C.M. Conrad, An Empirical Method for Estimating the Degree of Crystallinity of Native Cellulose Using the X-Ray Diffractometer, Text. Res. J. 29 (1959) 786–794. https://doi.org/10.1177/004051755902901003.

[43] M. Ashrafi, M. Arab Chamjangali, G. Bagherian, N. Goudarzi, Application of linear and non-linear methods for modeling removal efficiency of textile dyes from aqueous solutions using magnetic Fe3O4 impregnated onto walnut shell, Spectrochim. Acta - Part A Mol. Biomol. Spectrosc. 171 (2017) 268–279. https://doi.org/10.1016/j.saa.2016.07.049.

[44] M. Monier, D.A. Abdel-Latif, Preparation of cross-linked magnetic chitosan-phenylthiourea resin for adsorption of Hg(II), Cd(II) and Zn(II) ions from aqueous solutions, J. Hazard. Mater. 209–210 (2012) 240–249. https://doi.org/10.1016/j.jhazmat.2012.01.015.

[45] A. Salama, Functionalized hybrid materials assisted organic dyes removal from aqueous solutions, Environ. Nanotechnology, Monit. Manag. 6 (2016) 159–163. https://doi.org/10.1016/j.enmm.2016.10.003.

[46] R. Zhao, Y. Wang, X. Li, B. Sun, C. Wang, Synthesis of β-cyclodextrin-based electrospun nanofiber membranes for highly efficient adsorption and separation of methylene blue, ACS Appl. Mater. Interfaces. 7 (2015) 26649–26657. https://doi.org/10.1021/acsami.5b08403.

[47] Q. Wang, S. Liu, H. Chen, J. Liu, Q. Zhu, TEMPO-oxidized cellulose beads for cationic dye adsorption, BioResources. 17 (2022) 6056–6066. https://doi.org/10.15376/biores.17.4.6056-6066.

[48] L. Chen, Y. Li, S. Hu, J. Sun, Q. Du, X. Yang, Q. Ji, Z. Wang, D. Wang, Y. Xia, Removal of methylene blue from water by cellulose/graphene oxide fibres, J. Exp. Nanosci. 11 (2016) 1156–1170. https://doi.org/10.1080/17458080.2016.1198499.

[49] N. Mohammed, N. Grishkewich, R.M. Berry, K.C. Tam, Cellulose nanocrystal–alginate hydrogel beads as novel adsorbents for organic dyes in aqueous solutions, Cellulose. 22 (2015) 3725–3738. https://doi.org/10.1007/s10570-015-0747-3.

[50] H. Liu, X. Tian, X. Xiang, S. Chen, Preparation of carboxymethyl cellulose/graphene composite aerogel beads and their adsorption for methylene blue, Int. J. Biol. Macromol.

202 (2022) 632–643. https://doi.org/10.1016/j.ijbiomac.2022.01.052.

[51] D. Li, T. Hua, J. Yuan, F. Xu, Methylene blue adsorption from an aqueous solution by a magnetic graphene oxide/humic acid composite, Colloids Surfaces A Physicochem. Eng. Asp. 627 (2021) 127171. https://doi.org/10.1016/j.colsurfa.2021.127171.